Inorganic Chemistry

Article

Cite This: Inorg. Chem. 2019, 58, 9756−9765

pubs.acs.org/IC

Mononuclear Manganese(III) Superoxo Complexes: Synthesis, Characterization, and Reactivity

Yen-Hao Lin,[†] Hanna Hinrika Cramer,[§] Maurice van Gastel,[∥] Yi-Hsuan Tsai,[†] Chi-Yi Chu,[†] Ting-Shen Kuo,[‡] I-Ren Lee,*[,†] Shengfa Ye,*[,∥] Eckhard Bill,*[,§] and Way-Zen Lee*[,†]

[†]Department of Chemistry and [‡]Instrumentation Center, Department of Chemistry, National Taiwan Normal University, Taipei 11677, Taiwan

[§]Max-Planck-Institut für Chemische Energiekonversion, Mülheim an der Ruhr D-45470, Germany

[∥]Max-Planck-Institut für Kohlenforschung, Mülheim an der Ruhr D-45470, Germany

Supporting Information

ABSTRACT: Metal−superoxo species are typically proposed as key intermediates in the catalytic cycle of dioxygen activation by metalloenzymes involving different transition metal cofactors. In this regard, while a series of Fe−, Co−, and Ni−superoxo complexes have been reported to date, well-defined Mn−superoxo complexes remain rather rare. Herein, we report two mononuclear Mn^{III}−superoxo species, Mn(BDPP)($O_2^{\bullet-}$) (**2**, H_2BDPP = 2,6-bis((2-(*S*)-diphenylhydroxylmethyl-1-pyrrolidinyl)methyl)pyridine) and Mn($BDP^{Br}P$)($O_2^{\bullet-}$) (**2′**, $H_2BDP^{Br}P$ = 2,6-bis((2-(*S*)-di(4-bromo)phenylhydroxyl-methyl-1-pyrrolidinyl)methyl)-pyridine), synthesized by bubbling O_2 into solutions of their Mn^{II} precursors, Mn(BDPP) (**1**) and Mn($BDP^{Br}P$) (**1′**), at −80 °C. A combined spectroscopic (resonance Raman and electron paramagnetic resonance (EPR) spectroscopy) and computational study evidence that both complexes contain a high-spin Mn^{III} center (S_{Mn} = 2) antiferromagnetically coupled to a superoxo radical ligand ($S_{OO\bullet}$ = 1/2), yielding an overall S = 3/2 ground state. Complexes **2** and **2′** were shown to be capable of abstracting a H atom from 2,2,6,6-tetramethyl-1-hydroxypiperidine (TEMPO-H) to form Mn^{III}−hydroperoxo species, Mn(BDPP)(OOH) (**5**) and Mn($BDP^{Br}P$)(OOH) (**5′**). Complexes **5** and **5′** can be independently prepared by the reactions of the isolated Mn^{III}-aqua complexes, [Mn(BDPP)(H_2O)]OTf (**6**) and [Mn($BDP^{Br}P$)(H_2O)]OTf (**6′**), with H_2O_2 in the presence of NEt_3. The parallel-mode EPR measurements established a high-spin S = 2 ground state for **5** and **5′**.

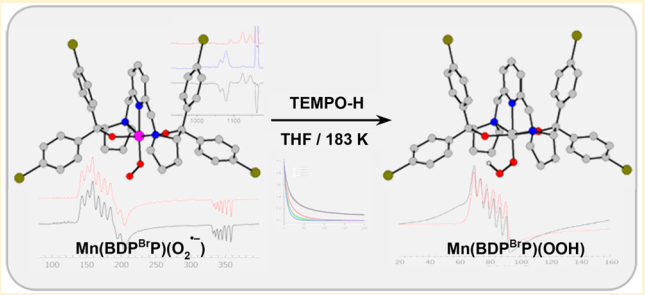

INTRODUCTION

Functionalization of organic compounds using O_2, a green oxidant, represents an essential process in nature.[1] Despite having favorable thermodynamic driving forces, direct substrate oxygenations usually have to traverse high kinetic barriers arising from the triplet-to-singlet spin inversion of O_2.[1] Nature has developed a diverse array of enzymes that contain transition metal cofactors to activate O_2; thus, metalloenzyme-catalyzed reactions typically proceed with unrivaled efficiencies under ambient conditions. The majority of O_2-activating wild-type enzymes utilize Fe and Cu in their active sites, whereas a few of them feature Mn and Ni. To the best of our knowledge, none of them incorporates Co. Catechol dioxygenases play a pivotal role in the global carbon cycle because they catalyze cleavage of aromatic rings and hence reclaim large quantities of carbon sequestered in ubiquitous aromatic compounds in nature.[2] Two forms of homoprotocatechuate 2,3-dioxygenases with the respective active-site metal ions being Fe^{II} and Mn^{II} have been isolated, namely, Fe-HPCD from *Brevibacterium fuscum*[3] and Mn-MndD from *Arthrobacter globiformis*.[4] Surprisingly, the native enzymes, Fe-HPCD and Mn-MndD, and their artificial variants, Mn-HPCD, Fe-MndD, and Co-HPCD, generated by reconstituting the native enzymes with nonphysiological metal ions, all exhibit comparable catalytic activity.[5] Therefore, it has long been believed that transition-metal-catalyzed oxidative transformations share common mechanistic features, in which O_2 initially binds to a reduced metal center to form an oxidized metal−superoxo species, which functions as the reagent to perform subsequent chemistry.[6] Isopenicillin *N* synthase (IPNS), an iron-dependent nonheme enzyme, which catalyzes formation of isopenicillin *N* en route to a number of important antibacterial drugs,[7] serves as a prototypical example for the proposed mechanism. O_2 association at the Fe^{II} center in IPNS has been experimentally shown to yield a Fe^{III}−superoxo intermediate, which initiates hydrogen atom abstraction (HAA) to generate presumably a hydroperoxo species (Scheme 1a).[8]

Notably, Fe^{III}− and Co^{III}−superoxo species were detected in the His200Asn mutant of Fe-HPCD and Co-HPCD in the

Received: March 18, 2019
Published: July 22, 2019

DOI: 10.1021/acs.inorgchem.9b00767
Inorg. Chem. 2019, 58, 9756−9765

Scheme 1. Mechanism of Dioxygen Activation by (a) IPNS, (b) Mn-HPCD, and (c) Model Complexes Supported by a $BDPP^{2-}$ or $BDP^{Br}P^{2-}$ Ligand

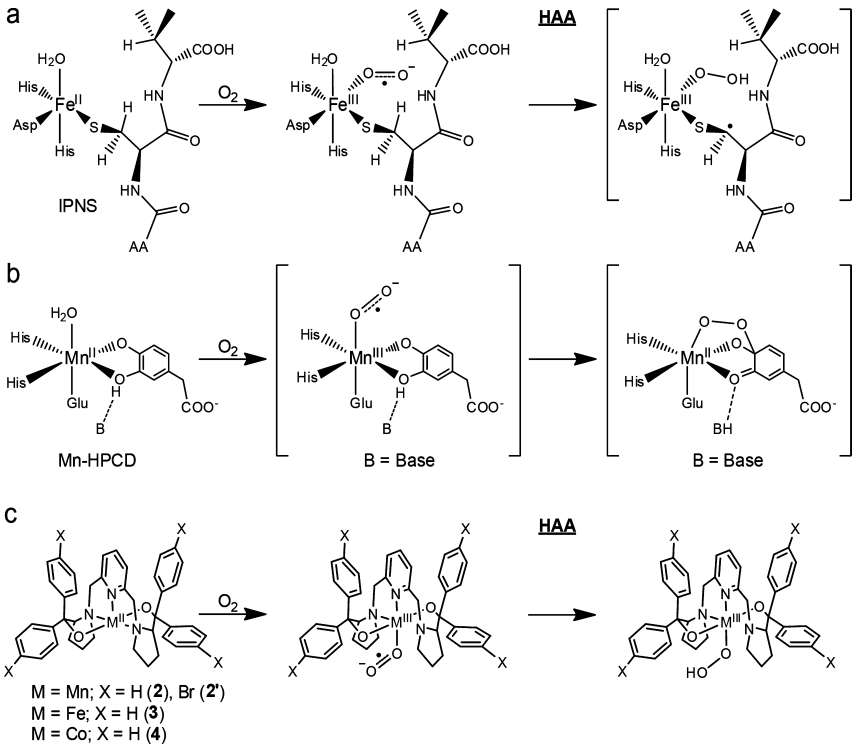

turnover of an electron-poor substrate, 4-nitocatechol.[9] Upon mixing of O_2 to Mn-HPCD, two intermediates were trapped and characterized by electron paramagnetic resonance (EPR) spectroscopy. They were assigned to a Mn^{III} ion coordinated by an unidentified radical, assumed to be a superoxo, and a Mn^{II}–alkylperoxo species (Scheme 1b), but the conclusive evidence remains elusive.[10] Furthermore, Mn^{III}–superoxo intermediates have been invoked in a series of Mn-catalyzed chemical transformations on the basis of the measurements using mass spectrometry,[11] and the existence of the putative Mn–superoxo species was postulated by investigations using low-temperature absorption spectroscopy[12] and reactivity studies.[13]

In addition to several synthetic nonheme Fe^{III}– and Co^{III}–superoxo models,[14−18] a Mn^{III}–superoxo complex, $[Mn^{III}(O_2)(OH_2)L]^{2+}$ (L = [5,11,17,23-tetrakis(trimethylammonium)-25,26,27,28-tetrahydroxylcalix[4]arene)]), has been crystallographically characterized to feature an unusual linear $Mn–O_2$ arrangement.[19] Its electronic structure has been probed by EPR and resonance Raman (rR) spectroscopy, and $[Mn^{III}(O_2)(OH_2)L]^{2+}$ was shown to exhibit catalytic reactivity toward alkene epoxidation. Unexpectedly, the determined $Mn^{III}–O_2$ bond distance (2.444 Å) is considerably longer than that of the trans $Mn–OH_2$ bond (2.210 Å). Notably, the Mn^{III}–O bond lengths found for $Mn–(O_2)$, Mn–OOR, and Mn–OR (R = H, Me, Ph, Ph-^{p}NO$_2$) species range from 1.832 to 1.901 Å (Table S1). Therefore, more work on well-defined Mn^{III}–superoxo complexes remains highly desirable due to the important roles played by such species in chemistry and biology.

Our earlier work reported synthesis and reactivity of nonheme Fe^{III}– and Co^{III}–superoxo complexes, Fe(BDPP)$(O_2^{\bullet-})$ (**3**) and Co(BDPP)$(O_2^{\bullet-})$ (**4**) (H_2BDPP = 2,6-bis((2-(*S*)-diphenylhydroxylmethyl-1-pyrrolidinyl)methyl)-pyridine).[14,16] Complexes **3** and **4** were synthesized by oxygenating the corresponding divalent metal precursors and found to be capable of performing HAA reactions (Scheme 1c). The aforementioned mechanistic hypothesis for O_2 activation prompted us to test the accessibility of the Mn^{III}–superoxo congeners via the same reaction route. To this end, we herein present the synthesis of two well-defined Mn^{III}–superoxo species and their spectroscopic characterizations as well as reactivity studies.

RESULTS AND DISSCUSSION

Synthesis and Characterization of Mn^{III}–Superoxo Complexes. Bubbling O_2 into THF or CH_2Cl_2 solutions of Mn(BDPP) (**1**) and Mn($BDP^{Br}P$) (**1′**) ($H_2BDP^{Br}P$ = 2,6-bis((2-(*S*)-di(4-bromo)phenylhydroxyl-methyl-1-pyrrolidinyl)-methyl)pyridine) at −80 °C results in a color change from pale yellow to deep yellow, due to the growth of three absorption bands at 370, 450, and 740 nm (Figures S4 and 1). This observation hints at the formation of $Mn–O_2$ adducts, Mn(BDPP)$(O_2^{\bullet-})$ (**2**) and Mn($BDP^{Br}P$)$(O_2^{\bullet-})$ (**2′**). Our repeated attempts to obtain single crystals of **2** and **2′** were foiled due to their gradual decomposition even at −80 °C.

The rR spectra (λ_{ex} at 457 nm) of **2**-^{16}O in CH_2Cl_2 reveal a Fermi doublet at 1125 and 1145 cm^{-1} (1135 cm^{-1} on average; see the inset in Figure 1a), which shifts to 1073 cm^{-1} upon ^{18}O substitution (99 atom %). The signals at 1125 and 1145 cm^{-1} in the **2**-^{18}O rR spectrum originate from trace $^{16}O_2$ contamination presumably coming from air during the sample preparation. The observed isotope shifts (62 cm^{-1}) are close to the value for a diatomic O–O bond stretching mode (ν_{O-O}) estimated by Hooke's law. In the case of **2′**, its ^{16}O rR spectrum (the inset in Figure 1b) also shows a doublet with exactly the same frequencies as those detected for **2**-^{16}O. Interestingly, its ^{18}O rR spectrum also demonstrates a different

DOI: 10.1021/acs.inorgchem.9b00767
Inorg. Chem. 2019, 58, 9756−9765

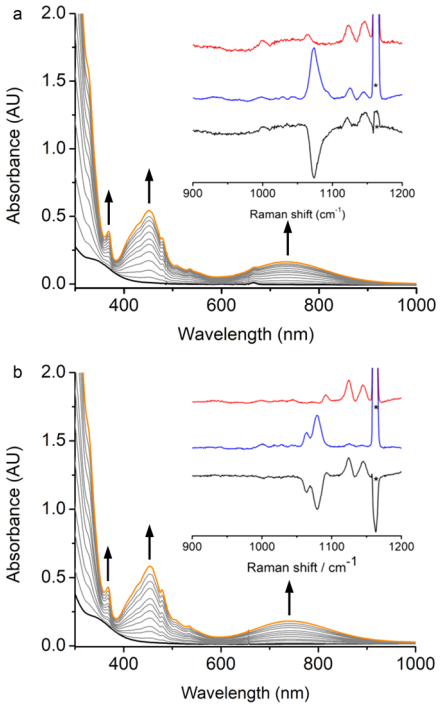

Figure 1. UV−vis spectra change for formation of (a) **2** and (b) **2′**. Complex **2** or **2′** (orange) from a reaction of **1** or **1′** (black, 0.4 mM) with O_2 in THF at −80 °C. Inset: rR spectra of **2** or **2′** (7.5 mM) in CH_2Cl_2 (λ_{ex} 457 nm, 10 mW, 77 K; red line: **2**-^{16}O or **2′**-^{16}O, blue line: **2**-^{18}O or **2′**-^{18}O, black line: difference spectrum **2**-^{16}O − **2**-^{18}O or **2′**-^{16}O − **2′**-^{18}O). Asterisks denote solvent peaks.

doublet at 1064 and 1078 cm^{-1}. The relative intensities of the two peaks of a given doublet measured for **2′**-^{16}O or **2′**-^{18}O are different, which essentially rules out the possibility that there exists two isomers for **2′**. On the basis of these observations, we attributed the two peaks observed for **2′**-^{16}O and **2′**-^{18}O to Fermi doublets. For the related Fe− and Cu−superoxo complexes, Fermi doublets arising from O−O stretching vibrations were typically found for either ^{16}O or ^{18}O samples,[15b,20a] but detection of both ^{16}O and ^{18}O Fermi doublets has been reported for a structurally characterized diiron(III)-μ-1,2-peroxo complex.[20b] The O−O stretching frequencies detected for **2** and **2′** closely match those reported for well-characterized metal−superoxo complexes (Table 1), thereby evidencing that **2** and **2′** accommodate a superoxo ligand.

In the following, we focus our discussion on **2′** because it has higher stability and solubility than those of **2** in MeTHF, and we summarize similar results of **2** in the Supporting Information. The X-band EPR spectrum of **2′** in MeTHF at 6.3 K (Figure 2) is typical for near-axial quartet systems with a

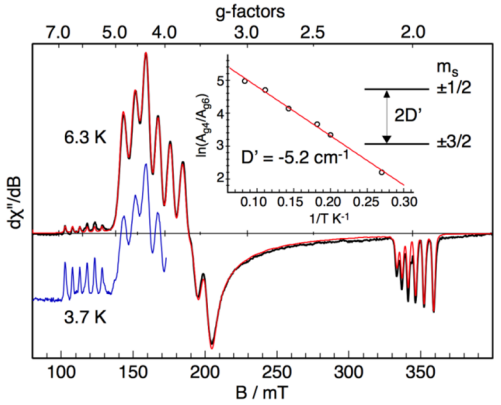

Figure 2. X-band EPR spectra of **2′** (2 mM) recorded at 6.3 K (black) and at 3.7 K (blue), and the simulation for 6.3 K (red). The simulation yields the following parameters: g_{iso} = 1.997(10), D = −5.2(5) cm^{-1}, E/D = 0.03(1), and $|A_{x,y,z}|$ = 234(10), 225(10), and 142(10) MHz. Note that the sign of the A values cannot determined experimentally. The inset shows the logarithm of the intensity ratio of the derivative signals $g_{eff} \approx 4$ and $g_{eff} \approx 6$ as a function of inverse temperature and a fit with the corresponding Boltzmann function (red line). Frequency 9.63595 GHz, power 0.2 mW, modulation 100 kHz/0.75 mT.

sizable axial zero-field splitting D and marginal rhombicity E/D ($|2D| \gg 0.3$ cm^{-1}, and $E/D \approx 0$). Specifically, the resonances of $g_{eff,\perp} \approx 4$ and $g_{eff,\parallel} \approx 2$ originate from the transition within its $M_S \approx \pm 1/2$ Kramers doublet. Consequently, the weak sextet around 115 mT can be attributed to the edge of the intra-Kramers doublet spectrum ($g_{eff,\parallel} \approx 6$ and $g_{eff,\perp} \to 0$) for the M_S

Table 1. O−O Stretching Frequencies of Mononuclear Metal Superoxo Complexes[a]

complex	ν(^{16}O−^{16}O), cm^{-1}	ν(^{18}O−^{18}O), cm^{-1}	$\Delta\nu$(O−O), cm^{-1}	ref
2	1125, 1145	1073	62	this work
2′	1125, 1145	1064, 1078	61	this work
$[Mn^{III}L(O_2^{\bullet-})(H_2O)](PF_6)_2$	1124	1035	89	19
3	1125	1062	63	14
4	1135	1070	65	16
$[Fe^{III}(TAML)(\eta^2\text{-}O_2^{\bullet-})]^{2-}$	1260	1183	77	15
$Fe^{III}(Tp^{Me2})(L^{Ph})(O_2^{\bullet-})$	1168	1090	78	17
$Co^{III}(Tp^{Me2})(L^{Ph})(\eta^1\text{-}O_2^{\bullet-})$	1150	1090	60	17
$Co^{III}(salen)(py)(O_2^{\bullet-})$	1144	1082	62	18
$[Cu^{II}(TMG_3tren)(\eta^1\text{-}O_2^{\bullet-})]^+$	1117	1059	58	21
$[Cu^{II}(6\text{-pivTPA})(O_2^{\bullet-})]^+$	1130	1067	63	22
$[Cr^{III}$ (14-TMC)$(\eta^1\text{-}O_2^{\bullet-})(Cl)]^+$	1170	1104	66	23

[a]L = 5,11,17,23-tetrakis(trimethylammonium)-25,26,27,28-tetrahydroxycalix[4]arene; TAML = 3,3,6,6,9,9-hexametyl-2,5,7,10-tetraoxo-3,5,6,7,9,10-hexahydro-2*H*-benzo[*e*][1,4,7,10]tetraazacyclotridecine-1,4,8,11-tetraide; Tp^{Me2} = hydro-tris(3,5-dimethylpyrazolyl)borate; L^{Ph} = bis(2-*N*-methylimizadolyl)methylphenylborate; salen = *N*,*N*′-ethylene-bis(salicylideneiminato); TMG_3tren = 1,1,1-tris(1-tetramethylguanidino)]-ethyl)amine); 6-pivTPA = (6-pivaloyl-amidopyridyl-2-methyl)bis(6-methylpyridyl-2-methyl)amine; 14-TMC = 1,4,8,11-tetramethyl-1,4,8,11-tetraazacyclo-tetradecane.

DOI: 10.1021/acs.inorgchem.9b00767
Inorg. Chem. 2019, 58, 9756−9765

$\approx \pm 3/2$ levels. The nicely resolved six lines at the $g_{eff,||} \approx 2$ and 6 and $g_{eff,\perp} \approx 4$ regions are due to the hyperfine coupling with ^{55}Mn ($I = 5/2$). From the relative intensity of the $g_{eff} \approx 4$ and 6 signals, the effective splitting $2D'$ ($D' = \sqrt{D^2 + 3E^2}$ of the quartet ground state was estimated to be $-10.4(5)$ cm^{-1} (see the inset in Figure 2).

The experimental EPR spectra of **2′** can be nicely fitted by using a usual spin-Hamiltonian for $S = 3/2$:

$$\hat{H} = D\left[\hat{S}_z^2 - \frac{1}{3}S(S+1) + \frac{E}{D}(\hat{S}_x^2 - \hat{S}_y^2)\right] + \beta\vec{B}g\hat{\vec{S}} + \hat{\vec{S}}A\hat{\vec{I}}$$

in which g is the intrinsic g matrix and A is the magnetic hyperfine coupling matrix. Double integration of the spectrum revealed nearly quantitative conversion of **1′** to **2′** in a yield of 96 (10)%.

The spectroscopic investigations suggest that **2′** is best formulated as a high-spin Mn^{III} ion ($S_{Mn} = 2$) bound to a $O_2^{\bullet-}$ radical ($S_{OO\bullet} = 1/2$) in an antiferromagnetic fashion yielding an overall quartet ground state ($S = 3/2$). As we will elaborate below, the exchange interaction in **2′** is in the strong coupling regime. The intrinsic D_{Mn} and A_{Mn} values of the Mn^{III} center in **2′** can be obtained from the effective D and A values determined experimentally for the total spin $S = 3/2$ ground state by using the relation $D = (7/5)D_{Mn}$ and $A = (6/5)A_{Mn}$.[24] The resulting intrinsic values, $D_{Mn} = -3.7$ cm^{-1} and $A_{Mn.iso} = 167$ MHz, fall into the range typically measured for distorted octahedral Mn^{III} complexes.[25] In contrast, an alternative formulation of **2′** as a high-spin Mn^{IV} complex ($S_{Mn} = 3/2$) can be safely ruled out, because well-characterized six-coordinate $S = 3/2$ Mn^{IV} compounds rarely feature negative D values and the magnitude of D never exceed 3 cm^{-1}, whereas negative D values are rather common for high-spin Mn^{III} complexes in elongated octahedral environments.[26] Experimentally, no signals that can be attributed to $S = 5/2$ have been observed up to 40 K, above which the fast relaxation induces significant line broadening of the EPR spectrum. Therefore, the exchange coupling constant between the high-spin Mn^{III} center and the superoxo ligand cannot be determined accurately.

Conversion of Mn^{III}–Superoxo Complexes to Mn^{III}–Hydroperoxo Complexes. Treating **2** and **2′** with 10 equiv of TEMPO-H in THF at −90 °C resulted in an exponential decay of their signature bands (Figures S7 and 3) and nearly quantitative yields of TEMPO radical (86% for **2**, Figure S8; 93% for **2′**, Figure S9). Our previous work showed that the reaction of the related Fe^{III}- and Co^{III}–superoxo complexes (**3** and **4**) with H-donor, DHA or TEMPO-H, produced the corresponding hydroperoxo species;[14,16] we thus surmised the products of the similar reactions with **2** and **2′** to be Mn^{III}–hydroperoxo species, Mn(BDPP)(OOH) (**5**) and Mn(BDP^{Br}P)(OOH) (**5′**). Treating the resulting solutions containing **5** and **5′** with HOTf followed by NaI allowed us to determine the yields of H_2O_2 to be 83% and 81%, respectively (Figures S11b and S12b).[27] The final products (Figures S11a and S12a) obtained by the acidified solution of **5** and **5′** were identified as Mn^{III}-aqua complexes, [Mn(BDPP)(H$_2$O)]OTf (**6**) and [Mn(BDP^{Br}P)(H$_2$O)]OTf (**6′**), which were characterized by X-ray crystallography (Figure 4). More importantly, complexes **5** and **5′** can be directly synthesized from the reactions of **6** and **6′** with an excess amount of a 2:1 mixture of H_2O_2 and NEt_3 in THF at −90 °C as monitored by electronic spectroscopy. As shown in Figures S13 and 5, upon

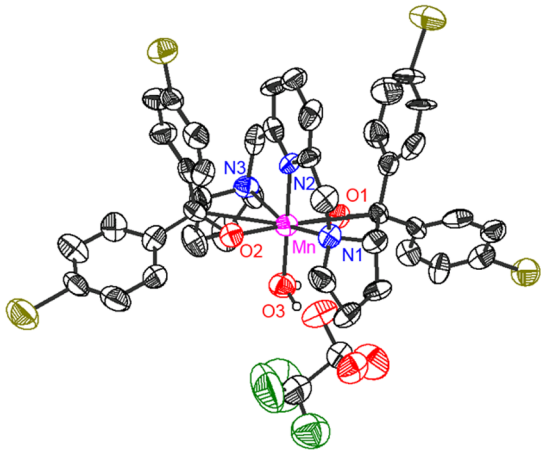

Figure 4. ORTEP presentation of [Mn(BDP^{Br}P)(H$_2$O)]OTf (**6′**). Hydrogen atoms are omitted for clarity. The Mn^{III} center of **6′** possesses an octahedral coordination environment. The important bond distances and angles of **6′** are as follows: Mn−N$_1$ = 2.248(7) Å, Mn−N$_2$ = 2.069(7) Å, Mn−N$_3$ = 2.255(7) Å, Mn−O$_1$ = 1.861(5) Å, Mn−O$_2$ = 1.881(5) Å, Mn−O$_3$ = 2.023(5) Å; ∠N$_1$−Mn−N$_2$ = 77.7(3)°, ∠N$_2$−Mn−N$_3$ = 79.1(3)°, ∠N$_1$−Mn−O$_3$ = 101.5(3)°, ∠N$_3$−Mn−O$_3$ = 101.7(3)°, ∠O$_1$−Mn−N$_2$ = 90.7(3)°, ∠O$_2$−Mn−N$_2$ = 91.3(2)°, ∠O$_1$−Mn−O$_3$ = 90.5(2)°, ∠O$_2$−Mn−O$_3$ = 87.5(2)°.

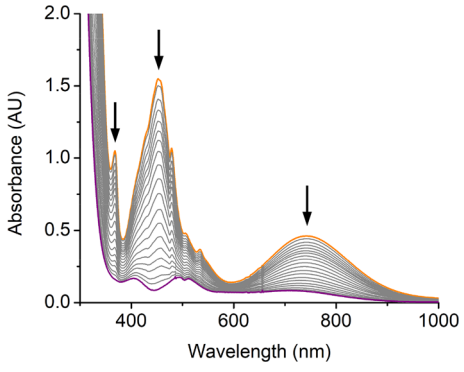

Figure 3. UV–vis spectra change monitored from the reaction of **2′** (orange line, 1 mM) with 10 equiv of TEMPO-H in THF at −90 °C. The purple line represents Mn(BDP^{Br}P)(OOH) (**5′**) with four absorption bands at 410, 495, 515, and 720 nm.

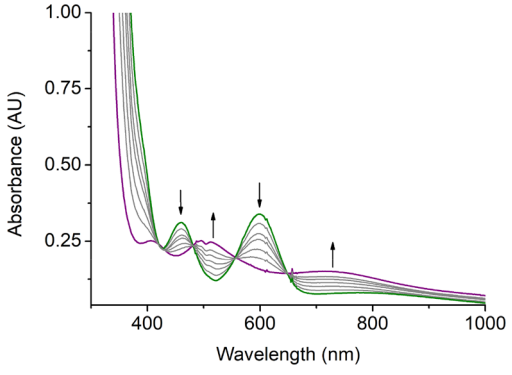

Figure 5. UV–vis spectra change monitored from the reaction of [Mn(BDP^{Br}P)(H$_2$O)]OTf (**6′**) (green line, 1 mM) with an excess amount of a 2:1 mixture of H_2O_2 and NEt_3 in THF at −90 °C. The purple line represents Mn(BDP^{Br}P)(OOH) (**5′**).

DOI: 10.1021/acs.inorgchem.9b00767
Inorg. Chem. 2019, 58, 9756−9765

addition of the mixture of H_2O_2 and NEt_3, the characteristic absorptions of **6** and **6′** at 460 and 600 nm gradually vanished along with the steady growth of those of **5** and **5′**. Our repeated attempts to obtain the O−O vibrational frequencies of **5** and **5′** from rR measurements failed, largely because **5** and **5′** have no intense chromophores in the usual UV−vis region (Figure 3) and the intensity of the O−O stretching signal is too low to be readily detected.

Figure 6 depicts a parallel-mode X-band EPR spectrum of **5′** in MeTHF at 10 K. Complex **5′** shows a six-line hyperfine

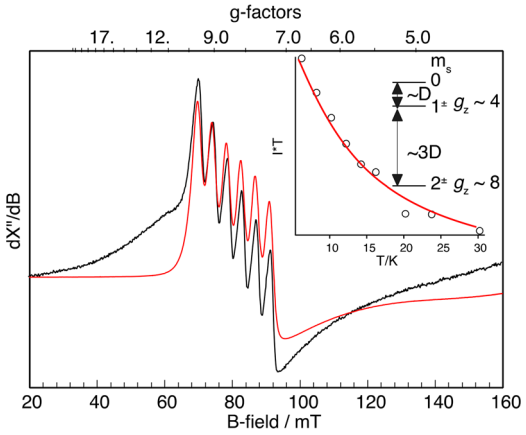

Figure 6. Parallel mode X-band EPR spectrum of **5′** (7.5 mM) recoded at 10 K (black) and the simulation (red). The inset shows signal intensity times temperature versus temperature of $g \sim 8$ signal (dots) and a fit with the corresponding Boltzmann function (red line). Frequency 9.396 GHz, power 0.2 mW, and modulation 100 kHz/0.75 mT.

pattern at $g \sim 8$ that stems from the transition within the $|2^{\pm}\rangle$ non-Kramers doublet of an $S = 2$ spin manifold, thus indicating that **5′** contains a high-spin Mn^{III} center. Its intensity declines with the temperature; hence, **5′** possesses a negative D value. The fit of the intensity variation as a function of temperature gives $D = -3.6(5)$ cm^{-1}. The resonance condition for this parallel-mode signal is $\hbar\nu = \sqrt{(4\mu_B g_{\parallel} B \cos\theta)^2 + \delta_{\pm 2}^2}$, where $\delta_{\pm 2} \approx \frac{3E^2}{D}$, $\hbar\nu$ is the microwave quanta, and θ is the angle between the magnetic field (B) and the z-axis of the D tensor. Moreover, its intensity is proportional to $\frac{g_{\parallel}^2 \delta_{\pm 2}^2}{(\hbar\nu)^2}$. Thus, one cannot simultaneously determine $g_{\parallel}$ and $\delta_{\pm 2}$ values accurately. During the simulation of the EPR spectrum, we therefore only allowed E/D to vary while fixing D to −3.6 cm^{-1} and g_{iso} to 2, the typical g value often found for related high-spin Mn^{III} complexes.[28] A satisfactory simulation yields the following parameters, $E/D = 0.09(1)$ and $|A_z| = 119(10)$ MHz. The broad underlying feature starting from ca. 60 mT is tentatively assigned to a high-spin Mn^{III} decay product since its relative intensity is dependent on the preparation. The onset of the signal at ca. 150 mT originates from small amount of O_2 in the solution.

Remarkably, the D and A_z values measured for complex **5′** are nearly identical to the intrinsic values of the Mn^{III} center found for **2′** ($D_{Mn} = -3.7$ cm^{-1} and $A_{Mn,z} = 118$ MHz), thereby suggesting that the Mn^{III} centers in both complexes feature a similar electronic structure and are ligated in an analogous coordination environment. All these observations confirm that **5** and **5′** are indeed high-spin Mn^{III}−hydroperoxo species. Unlike **5** and **5′**, **6** and **6′** were found to be EPR-silent in both normal and parallel modes (Figure S10). This finding likely reflects a considerable change in the electronic structure induced by replacing an anionic hydroperoxo ligand with H_2O.

DFT Calculations of 2′ and 5′. In order to better understand the nature of **2′** and **5′**, detailed computational studies on **2′** and **5′** were undertaken. Complex **2′** was predicted to have a quartet ground state, and the lowest-energy sextet state in which the high-spin Mn^{III} center is ferromagnetically coupled to the superoxo ligand is situated at ∼1300 cm^{-1} higher in energy. The optimized quartet structure of **2′** features elongated octahedral coordination geometry. The two Mn−$N_{pyrrolidine}$ bonds along the z direction are substantially longer than all of the metal−ligand bond distances in the equatorial plane (Figure 7). The different metal−ligand bond lengths

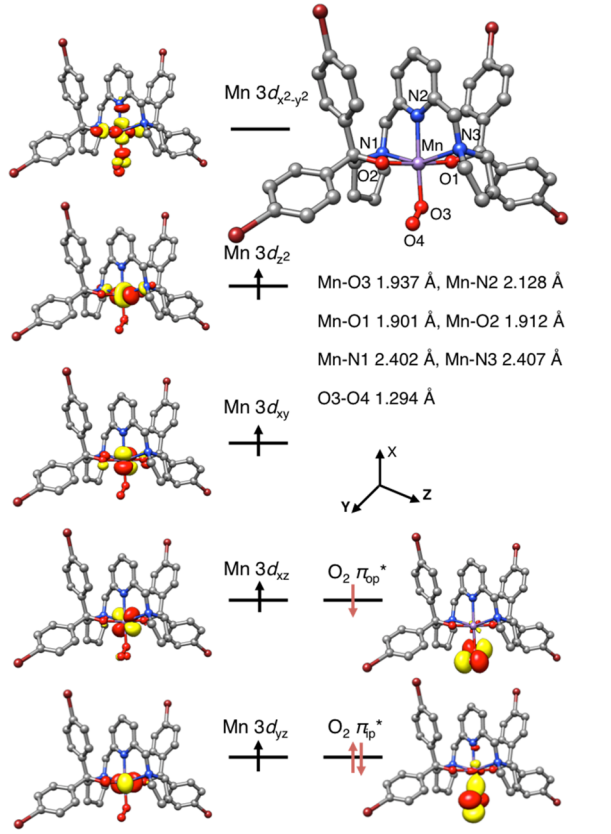

Figure 7. Computed structure of **2′** with key geometric parameters and its schematic molecular orbital diagram.

simply reflect the fact that the equatorial plane consists of three negatively charged O donors and a rigidly chelated $N_{pyridine}$ atom, whereas there are two neutral $N_{pyrrolidine}$ donors in the axial direction. In keeping with this reasoning, the Mn^{III} center features an electron configuration of $(d_{yz})^1(d_{xz})^1(d_{xy})^1(d_{z^2})^1(d_{x^2-y^2})^0$, in which the Mn^{III} $d_{x^2-y^2}$ based molecular orbital is vacant. The calculated O−O distance (1.294 Å) of the O_2 moiety agrees with those found in structurally characterized metal−superoxo complexes (Table S2). Furthermore, one of the two O_2 π^* orbitals is doubly occupied, and the other is resided by a β-electron. Such an orbital occupation pattern defines a high-spin Mn^{III} ion ($S_{Mn} = 2$) that is antiferromagnetically coupled to a superoxo radical ($S_{OO\bullet} = 1/2$).

DOI: 10.1021/acs.inorgchem.9b00767
Inorg. Chem. 2019, 58, 9756−9765

Complex **5′** also features an elongated octahedral coordination arrangement with the two considerably longer Mn−$N_{pyrrolidine}$ bonds, similar to that of **2′** (Figure 8). Consequently,

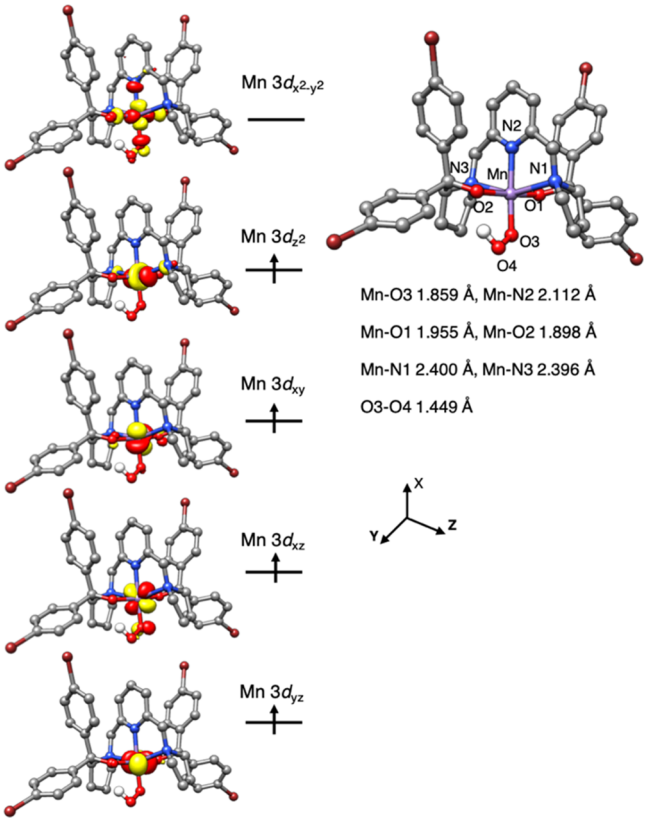

Figure 8. Computed structure of **5′** with key geometric parameters and its schematic molecular orbital diagram.

the Mn^{III} centers in both complexes possess the same electron configuration. Relative to **2′**, the estimated O−O distance of the OOH unit in **5′** is significantly lengthened to 1.449 Å, a typical O−O bond length observed for metal−hydroperoxo species.[16] Furthermore, the hydroperoxo ligand forms a hydrogen bond with one of the O atom of $BDP^{Br}P$, analogous to hydrogen bonding observed in the crystal structure of Co(BDPP)(OOH). Our theoretical results revealed that such interaction stabilizes **5′** by 5.3 kcal/mol relative to another isomer, in which the H atom in the OOH ligand points out of the O2 atom of $BDP^{Br}P$. Moreover, the computed spectroscopic parameters for **2′** and **5′** and the O−O stretching frequency for **2′** (1162 cm^{-1}) match the experimental data within the uncertainty range of the calculations, which further lends credence to the proposed geometric and electronic structures for them (Table S3).

The weak axial coordination found for the Mn^{III} centers in complexes **2′** and **5′** is consistent with the observed negative *D* values and the relative magnitude of the three *A* components ($|A_x| \approx |A_y| < |A_z|$) (for details, see the Supporting Information). In fact, $[Mn^{III}(O_2)(OH_2)L]^{2+}$ features the same coordination geometry as that of **2′**, but the distortion was found along the O_2−Mn−OH_2 axis,[19] because the bowl-shaped calix[4]arene ligand with four phenolate groups predefines an equatorial plane and forces the superoxo ligand to coordinate the Mn^{III} center in the axial position.

Reactivity Comparisons of O_2 Activations by Mn, Fe, and Co Counterparts. Our findings reveal that **2** and **2′** can be prepared by using the same synthetic route as that for their Fe and Co counterparts, **3** and **4**.[14,16] However, under the same experimental conditions, formation of **4** (~0.26 min^{-1} in THF, even slower rate in CH_2Cl_2) is at least 10-fold slower than that of **2′** and **3**, a situation similar to that observed for O_2 binding to Co- and Fe-HPCD.[9] Unexpectedly, the relative formation rates of **2′**, **3**, and **4** do not follow the trend of the redox potentials of their divalent precursors ($[Mn^{II}(BDPP)]^{0/+}$, −0.555 V; $[Fe^{II}(BDPP)]^{0/+}$, −0.328 V; $[Co^{II}(BDPP)]^{0/+}$, −0.476 V vs Fc/Fc^+). Thus, we reason that the difference mainly results from the unavoidable spin transition from a high-spin Co^{II} in Co(BDPP) to a low-spin Co^{III} in **4**, whereas such processes are not required for the generation of **2**, **2′**, and **3**. Bubbling N_2 into a THF solution of **3** at −80 °C leads to O_2 dissociation,[14] whereas analogous interconversion processes have not been found for **2**, **2′** (Figure S5), and **4**. This observation suggests that the metal−superoxo bonding is weaker in **3** than that in **2**, **2′**, and **4**, consistent with the Fe−$O_2^{\bullet-}$ distance computed for **3** being considerably longer than those for **2**, **2′**, and **4** (Table S4).

Complex **3** is capable of performing HAA toward dihydroanthracene[14] (DHA, D_{C-H} 78 kcal/mol[29]), whereas no reaction was observed when mixing **2**, **2′**, and **4** with DHA. Instead, **4** was shown to convert 2,2,6,6-tetramethyl-1-hydroxypiperidine (TEMPO-H), a more potent H atom donor (D_{O-H} 69.7 kcal/mol[29]), to TEMPO radical via HAA.[16] Relative to **4**, superior HAA efficacy is found for **2′**, which breaks the O−H bond at least 500-fold faster. Owing to the rapid reaction rate of **2′** with a large excess of TEMPO-H, where pseudo-first-order reaction kinetics was beyond the temporal resolution of our apparatus, we then performed a kinetic titration experiment with *n* equiv of TEMPO-H ($n \sim 0.8-2.0$). Second-order reaction kinetics was confirmed by the excellent agreement of experimental data and the model below, as shown in Figure 9:

$$\frac{[A]_t}{[A]_0} = \frac{n-1}{n\exp((n-1)[A]_0 kt) - 1}$$

where $[A]_0$ and $[A]_t$ represent the concentrations of **2′** before and at a given time *t* after the addition of TEMPO-H, respectively. The ratio $[A]_t/[A]_0$ was obtained from the normalized transient absorption signal of **2′**. An initial concentration of **2′** ($[A]_0 = 1.86 \times 10^{-4}$ M, 93% yield from the EPR data) was applied in the nonlinear least-squared fitting, and the exact *n* value (for details, see the Supporting Information) and the rate constant, *k*, were obtained. The second-order rate constant of this reaction, $k_2 = 500 \pm 60$ M^{-1} s^{-1}, was deduced from the average of 4 independent measurements. Deuterated TEMPO-D was examined similarly. Linear plots (inset of Figure 9) were derived according to the following kinetic equation for both TEMPO-H and TEMPO-D at the concentration around 1.2 equiv to **2′**.

$$y = \frac{1}{(n-1)[A]_0}\ln\left[\frac{n-1}{n}\frac{[A]_0}{[A]_t} + \frac{1}{n}\right] = kt$$

A KIE value of 1.5 was obtained, suggesting that the homolytic O−H bond cleavage does not make the major contribution to the reaction coordinate of the rate-determining step for the conversion of Mn^{III}-superoxo **2′** to Mn^{III}-hydroperoxo **5′**.

DOI: 10.1021/acs.inorgchem.9b00767
Inorg. Chem. 2019, 58, 9756−9765

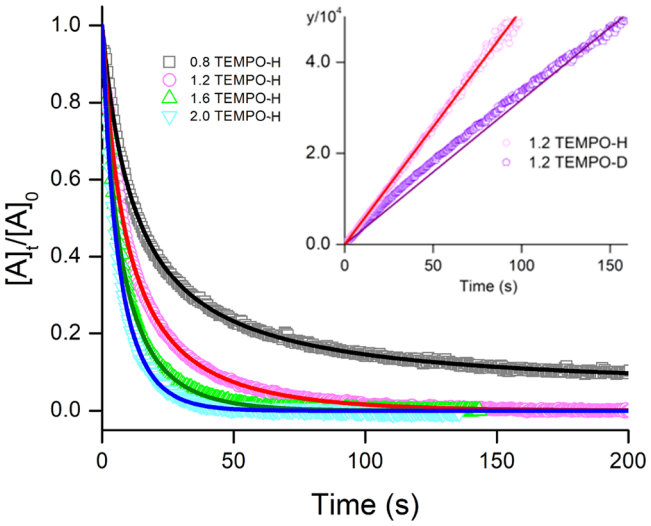

Figure 9. Nonlinear least-squared fitting for the reaction traces of **2′** in THF with various equiv of TEMPO-H monitored by UV−vis spectroscopy. The inset shows the linear plots of TEMPO-H and TEMPO-D following kinetic equation at the concentration around 1.2 equiv to **2′**.

Obviously, complexes **2′**, **3**, and **4** exhibit differential HAA activity due to the nature of the individual metal center. After adjustment for differences in temperature and substrate D_{C-H} values, it appears that **2′** has a rate for HAA toward TEMPO-H much faster than those of Co(BDPP)($O_2^{\bullet-}$) (**4**, k_2 = 0.97 M^{-1} s^{-1} at −90 °C), [$L^1Cu^{II}(O_2^{\bullet-})$]$PF_6$ (L^1 = 1-(2-phenethyl)-5-[2-(2-pyridyl)ethyl]-1,5-diazacyclooctane, k_2 = 2.4 M^{-1} s^{-1} at −85 °C),[30] [$L^2Cu^{II}(\mu$-1,2-$O_2^{\bullet-}$)]BPh_4 (L^2 = tacn/pyrazolate hybrid ligand, k_2 = 0.254 M^{-1} s^{-1} at −10 °C),[31] and [K(Krypt)][$L^3Cu(O_2^{\bullet-})$] (L^2 = a bis(arylcarboxamido)-pyridine ligand, k_2 = 34.9 M^{-1} s^{-1} at −80 °C).[32]

CONCLUSION

Mononuclear Mn^{III}−superoxo complexes **2** and **2′** were synthesized by reacting O_2 with precursors **1** and **1′** at −80 °C. Our combined spectroscopic and computational study reveals that **2** and **2′** are best formulated as a high-spin Mn^{III} center antiferromagnetically coupled to a superoxo ligand yielding an overall quartet ground state. Complexes **2** and **2′** were shown to activate a weak O−H bond of TEMPO-H to generate Mn^{III}−hydroperoxo complexes **5** and **5′**. Notably, complex **2′** cleaves the O−H bond in TEMPO-H much faster than the reported Co- and Cu−superoxo complexes.[30−32] Acidification of **5** and **5′** produces nearly quantitative H_2O_2 and Mn^{III}-aqua complexes **6** and **6′**. Conversely, complexes **5** and **5′** can be directly prepared from the reactions of **6** and **6′** with an excess amount of a 2:1 mixture of H_2O_2 and NEt_3 in THF at −90 °C.

Our earlier work showed that similar to **2** and **2′** their Fe^{III} and Co^{III} congeners (**3** and **4**) can be prepared in the same way and that the resulting trivalent metal−superoxo complexes can initiate HAA reactions and produce trivalent metal−hydroperoxo complexes. All these findings provide direct experimental support for the proposed mechanism for O_2 activation by distinct transition metals. Despite this, the three metal centers display different O_2 bonding rates, and O_2 adducts **2′**, **3**, and **4** exhibit distinct metal−superoxo bonding strengths and HAA activities. The observations warrant further systematic investigations devoting to pinpoint key features responsible for the metal specificity.

EXPERIMENTAL SECTION

Materials and Methods. All manipulations are performed under N_2 conditions using glovebox or Schlenk techniques. Acetonitrile was purified by the MBraun Solvent Purification System (MB-SPS). Diethyl ether, THF, and pentane were dried by sodium/benzophenone and distilled prior to use. Dichloromethane were dried by CaH_2 and distilled prior to use. 2,6-Bis(((*S*)-2-diphenylhydroxymethyl-1-pyrolidinyl)methyl)pyridine (H_2BDPP), 2,6-bis(((*S*)-2(bis(4-bromophenyl)hydroxyl-methyl-1-pyrolidinyl)methyl)pyridine ($H_2BDP^{Br}P$), and 2,2,6,6-tetramethyl-1-hydroxypiperidine (TEMPO-H) were synthesized according to the literature methods.[33] All the other chemical reagents were obtained from commercial sources and used without purification. UV−vis spectra were recorded with Agilent 8453 spectrophotometer equipped with cryostat from Unisoku Scientific Instruments, Osaka, Japan. Elemental analyses for C, H, and N were performed on an elementar Vario EL cube analyzer at the Instrumentation Center in National Taiwan University.

X-ray Data Collection and Structure Determination. X-ray diffraction data of crystals of **1**, **1′**, and **6′** were collected on a Bruker Kappa APEX II CCD diffractometer employing Mo Kα radiation (λ = 0.7107 Å) at 200 K and with a θ−2θ scan mode. The space groups for **1**, **1′**, and **6′** were determined on the basis of systematic absences and intensity statistics. Their structures were solved by direct methods using SIR92 or SIR97, and refined using SHELXL-97 with anisotropic displacement factors for all non-hydrogen atoms. For X-ray structures of **1′** and **6′**, half or one CH_2Cl_2 solvent molecule in **1** and one Et_2O solvent molecule in **6′** per unit cell are squeezed by PLATON program. The detailed crystallographic data of **1**, **1′**, and **6′** were provided in their crystallographic information files.

EPR Measurements. X-band cw-EPR measurements were performed on a Bruker E500 ELEXSYS spectrometer equipped with the Bruker dual-mode cavity (ER4116DM) and an Oxford Instruments helium flow cryostat (ESR 900). The microwave bridge was the high-sensitivity bridge Super-X from Bruker (ER-049X) with integrated microwave frequency counter. The magnetic field controller (ER032T) was externally calibrated with a Bruker NMR field probe (ER035M). Spectral analysis and simulations were handled by using the EasySpin program.[34]

Resonance Raman Collections. Resonance Raman spectra were recorded on a TriVista 555 triple monochromator equipped with a liquid-nitrogen-cooled Roper Scientific 400BR Excelon CCD camera. An excitation wavelength of 457 nm and 10 mW from a cobalt solid-state laser was used. The solution of a sample was packed into a quartz EPR tube and measured in an EPR quartz finger Dewar which was cooled with liquid nitrogen. The Raman signal was collected in a 180° backscattering geometry with a Thorlabs MPD249H−P01 off-axis parabolic mirror and focused onto the entrance slit of a spectrograph with a 100 mm diameter f/4 lens. The scattered light was dispersed with a grating of 1800 mm^{-1} and further with two filter prestages of 900 mm^{-1}. The slit widths at the first and third stages amounted to 100 μm, thus providing a spectral resolution at the CCD camera of about 0.8 cm^{-1}. Spectra were collected for about 30 min for a given wavelength and spectral window. Calibration of the Raman shifts has been achieved to an accuracy of 1 cm^{-1} by using Na_2SO_4 as well as the solvent signals as references.

Synthesis of Mn(BDPP) (1) and Mn($BDP^{Br}P$) (1′). Mn(BDPP) (**1**) was synthesized by reacting $Mn(OTf)_2$ (141.2 mg, 0.4 mmol) with H_2BDPP (244.0 mg, 0.4 mmol) and NaH (24.0 mg, 1.0 mmol) in 15 mL of CH_3CN in a 50 mL Schlenk flask. The solution was stirred for 3 h at ambient temperature and then vacuumed. The pale yellow residue was dissolved in CH_2Cl_2 (20.0 mL) and filtered. The filtrate was concentrated under vacuum and recrystallized by slow diffusion of Et_2O into the concentrated CH_2Cl_2 filtrate at ambient temperature. Yellow crystals of **1** were obtained in 55% yield over 1 day. The structure of **1** features a distorted square pyramidal geometry (τ_5 = 0.45). UV−vis (THF): 338 nm (450 M^{-1} cm^{-1}). Anal. Calcd

DOI: 10.1021/acs.inorgchem.9b00767
Inorg. Chem. 2019, 58, 9756−9765

for $C_{41}H_{41}MnN_3O_2$ (F.W. = 662.71): C, 69.35; H, 5.92; N, 5.82. Found: C, 69.509; H, 6.176; N, 6.121. The synthesis of Mn(BDP^{Br}P) (**1′**) is similar to the procedures for that of **1** ($Mn(OTf)_2$: 0.1412 g, 0.4 mmol; $H_2BDP^{Br}P$: 0.3770 g, 0.4 mmol; NaH: 0.024 g, 1.0 mmol). Slow diffusion of pentane into the THF solution of **1′** at ambient temperature was performed for recrystallization. Yellow crystals of **1′** were obtained in 50% yield over 1 day. The structure of **1′** features a distorted square pyramidal geometry (τ_5 = 0.34). UV−vis (THF): 350 nm (322 M^{-1} cm^{-1}). Anal. Calcd for $C_{41}H_{37}Br_4MnN_3O_2$·THF (F.W. = 1050.43): C, 51.45; H, 4.32; N, 4.00. Found: C, 51.587; H, 4.463; N, 3.801.

Formation of Mn(BDPP)($O_2^{\bullet-}$) (2) and Mn(BDP^{Br}P)($O_2^{\bullet-}$) (2′). Complexes **2** and **2′** were generated by bubbling O_2 into THF or CH_2Cl_2 solutions of **1** and **1′** at −80 °C from an oxygen balloon for 2 min. Formation of **2** and **2′** was monitored by UV−vis spectroscopy on characteristic absorption bands at 370, 450, and 740 nm. We found that the volume of O_2 in the balloon and the elasticity of the balloon have a large influence on the formation rate of **2** and **2′**, a situation similar to that encountered for Fe(BDPP)($O_2^{\bullet}$) (**3**), indicating that the formation of **2** and **2′** is rapid and close to the diffusion rate of O_2 in the working solutions.

Production of Mn^{III}(BDPP)(H_2O)(OTf) (6) and Mn^{III}(BDP^{Br}P)(H_2O)(OTf) (6′) from Protonation of 5 and 5′. Complex **6** was produced from the reaction of **5** (0.2 mmol) with 1 equiv of HOTf at −90 °C then warming up to room temperature. After 3 h, the resulting green solution was evaporated. The crude powder was redissolved in mixed THF/CH_3CN (10:1). Pentane was then added to the mixing THF/CH_3CN solution to obtain a green precipitate of **6** which was isolated in a yield of 116.2 mg (70%). Complex **6′** was prepared with the same procedure. Crystallization of **6′** gave a yield of 169.5 mg (74%). Anal. Calcd for C_{42} H_{39} Br_4 F_3 Mn N_3 O_6 S·$0.5C_4H_8O$ (F.W. = 1182.46): C, 44.69; H, 3.75; N, 3.55; S, 2.71. Found: C, 44.50; H, 3.91; N, 3.47; S, 2.52.

Preparation of Mn(BDPP)(OOH) (5) and Mn(BDP^{Br}P)(OOH) (5′) from Reactions of 6 and 6′ with a Mixture of H_2O_2/NEt_3. A solution of basic hydrogen peroxide (10 equiv of H_2O_2 with 5 equiv of NEt_3, 100 μL) was added to a THF solution of **6** (1.0 mM, 3.0 mL) at −90 °C. The color of the reaction solution changed from green to pale purple exhibiting the formation of **5**. Meanwhile, the absorption bands of **6** at 460 and 600 nm declined, and the bands of **5** at 510 and 720 nm grew as monitored by the UV−vis spectroscopy. Complex **5′** was prepared by the same procedure.

Kinetic Study of 2′ toward TEMPO-H. TEMPO-H (1.0, 1.5, 2.0, and 2.5 equiv) was added to a THF solution of **2′** at −90 °C. The reacting solution was monitored by UV−vis spectroscopy, and a rapid decline of the absorption band at 450 nm was recorded. Each condition was examined three times. Reaction of **2′** with 1.5 equiv of TEMPO-D was also performed, and the rate was obtained to derive the kinetic isotope effect (KIE) value.

Computational Details. Geometry optimizations and frequency calculations were carried out with the B3LYP density functional.[35] The triple-ζ quality basis set, def2-TZVP,[36] was used for Mn and the atoms in the first coordination sphere, while the remaining atoms were treated with def2-SVP[37] basis set. The calculations were accelerated by using RI (resolution of the identity) approximation,[38,39] for which the auxiliary coulomb-fitting basis set def2-TZVP/J[38] was used. All geometry optimizations were performed incorporating solvation effect through conductor-like polarizable continuum model (CPCM)[40] with the solvent THF (ε = 7.25). The noncovalent interactions were accounted for through atom-pairwise dispersion corrections with Becke−Johnson (D3BJ)[41] damping.

Spectroscopic parameters were computed by using the TPSSh density functional[42] in combination with the CP(PPP) basis set for Mn,[43] the def2-TZVP basis set for the atoms in the first coordination sphere, and the def2-SVP for the remaining atoms. The magnetic hyperfine coupling matrix, **A**, of the ^{55}Mn center was calculated by taking the isotropic Fermi contact term, the first-order traceless dipolar contribution, and the second-order nontraceless spin−orbit contribution into account. The Fermi-contact contributions were scaled by a factor of 1.49.[44] Spin−orbit contributions to the hyperfine tensors were calculated as second order properties employing the coupled perturbed (CP) Kohn−Sham theory.[45] The Mn magnetic hyperfine coupling constants of the "genuine" antiferromagnetic state A_i^{AF} were calculated from the magnetic hyperfine coupling constants of the corresponding broken symmetry state A_i^{BS} by conversion into "site values" and multiplication with the spin projection coefficients C_i:[46]

$$A_i^{AF} = C_i \frac{A_i^{BS} M_s^{BS}}{\pm S_i}$$

The contributions of spin orbit coupling (SOC) to the zero-field splitting (ZFS)[24] were calculated by linear response theory.[47]

The spin−spin coupling contributions to ZFSs are calculated from the equation of McWeeny and Mizuno.[48]

$$D_{kl}^{SS} = \frac{g_e^2}{4}\frac{\alpha^2}{S(2S-1)}\sum_{\mu\nu}\sum_{\kappa\tau}\{\mathbf{P}_{\mu\nu}^{\alpha-\beta}\mathbf{P}_{\kappa\tau}^{\alpha-\beta} - \mathbf{P}_{\mu\kappa}^{\alpha-\beta}\mathbf{P}_{\nu\tau}^{\alpha-\beta}\}$$
$$\langle\mu\nu|r_{12}^{-5}\{3r_{12,k}r_{12,l} - \delta_{kl}r_{12}\}|\kappa\tau\rangle$$

in which spin density matrix $\mathbf{P}^{\alpha-\beta}$ was obtained on the basis of the spin-unrestricted natural orbital (UNO) determinant.[49] All calculations were performed by using the ORCA quantum chemical program package.[50]

■ ASSOCIATED CONTENT

Supporting Information

The Supporting Information is available free of charge on the ACS Publications website at DOI: 10.1021/acs.inorgchem.9b00767.

UV−vis, NMR and HRMS spectra of **1**−**3**, EPR spectra of **1**−**2**, and computational result of **1** (PDF)

Accession Codes

CCDC 1898662−1898664 contain the supplementary crystallographic data for this paper. These data can be obtained free of charge via www.ccdc.cam.ac.uk/data_request/cif, or by emailing data_request@ccdc.cam.ac.uk, or by contacting The Cambridge Crystallographic Data Centre, 12 Union Road, Cambridge CB2 1EZ, UK; fax: +44 1223 336033.

■ AUTHOR INFORMATION

Corresponding Authors

*E-mail: wzlee@ntnu.edu.tw (W.-Z.L.).
*E-mail: shengfa.ye@kofo.mpg.de (S.Y.).
*E-mail: eckhard.bill@cec.mpg.de (E.B.).
*E-mail: irenlee @ntnu.edu.tw (I.-R.L.).

ORCID

Maurice van Gastel: 0000-0002-1547-6365
I-Ren Lee: 0000-0001-5655-6049
Shengfa Ye: 0000-0001-9747-1412
Eckhard Bill: 0000-0001-9138-3964
Way-Zen Lee: 0000-0003-0053-1621

Notes

The authors declare no competing financial interest.

■ ACKNOWLEDGMENTS

We thank Mr. Dennis Skerra at the Max-Planck Institute for Chemical Energy Conversion for resonance Raman measurements. We are grateful for the financial support from the Ministry of Science and Technology of Taiwan (MOST 105-2113-M-003-005-MY3 to W.-Z.L.) and the Max-Planck Society, in particular, the joint work space between MPI-CEC and MPI-KOFO. W.-Z.L. and S.Y. also acknowledge the

DOI: 10.1021/acs.inorgchem.9b00767
Inorg. Chem. 2019, 58, 9756−9765

MOST-DAAD Project-Based Personnel Exchange Program (MOST 107-2911-I-003-502 and DAAD 57320810).

REFERENCES

(1) Bertini, I.; Gray, H. B.; Lippard, S. J.; Valentine, J. S. Dioxygen Reactions. In *Bioinorganic Chemistry*; University Science Books: Mill Valley, CA, 1994; pp 253−313.

(2) (a) Costas, M.; Mehn, M. P.; Jensen, M. P.; Que, L. DiOxygen Activation at Mononuclear Non-Heme Iron Active Sites: Enzymes, Models, and Intermediates. *Chem. Rev.* **2004**, *104*, 939−986. (b) Vaillancourt, F. H.; Bolin, J. T.; Eltis, L. D. The Ins and Outs of Ring-Cleaving Dioxygenases. *Crit. Rev. Biochem. Mol. Biol.* **2006**, *41*, 241−267. (c) Kovaleva, E. G.; Lipscomb, J. D. Versatility of Biological Non-heme Fe(II) Centers in Oxygen Activation Reactions. *Nat. Chem. Biol.* **2008**, *4*, 186−193.

(3) Miller, M. A.; Lipscomb, J. D. Homoprotocatechuate 2,3-Dioxygenase from Brevibacterium fuscum. *J. Biol. Chem.* **1996**, *271*, 5524−5535.

(4) Whiting, A. K.; Boldt, Y. R.; Hendrich, M. P.; Wackett, L. P.; Que, L. Manganese(II)-Dependent Extradiol-Cleaving Catechol Dioxygenase from *Arthrobacter Globiformis* CM-2. *Biochemistry* **1996**, *35*, 160−170.

(5) (a) Emerson, J. P.; Kovaleva, E. G.; Farquhar, E. R.; Lipscomb, J. D.; Que, L., Jr. Swapping Metals in Fe- and Mn-Dependent Dioxygenases: Evidence for Oxygen Activation without a Change in Metal Redox State. *Proc. Natl. Acad. Sci. U. S. A.* **2008**, *105*, 7347−7352. (b) Fielding, A. J.; Kovaleva, E. G.; Farquhar, E. R.; Lipscomb, J. D.; Que, L., Jr. A Hyperactive Cobalt-substituted Extradiol-cleaving Catechol Dioxygenase. *JBIC, J. Biol. Inorg. Chem.* **2011**, *16*, 341−355.

(6) (a) Solomon, E. I.; Brunold, T. C.; Davis, M. I.; Kemsley, J. N.; Lee, S.-K.; Lehnert, N.; Neese, F.; Skulan, A. J.; Yang, Y.-S.; Zhou, J. Geometric and Electronic Structure/Function Correlations in Non-Heme Iron Enzymes. *Chem. Rev.* **2000**, *100*, 235−349. (b) Huang, X.; Groves, J. T. Beyond Ferryl-Mediated Hydroxylation: 40 Years of the Rebound Mechanism and C−H Activation. *JBIC, J. Biol. Inorg. Chem.* **2017**, *22*, 185−207.

(7) Baldwin, J. E.; Bradley, M. Isopenicillin N Synthase: Mechanistic Studies. *Chem. Rev.* **1990**, *90*, 1079.

(8) Tamanaha, E.; Zhang, B.; Guo, Y.; Chang, W.-c.; Barr, E. W.; Xing, G.; St. Clair, J.; Ye, S.; Neese, F.; Bollinger, J. M.; Krebs, C. Spectroscopic Evidence for the Two C−H-Cleaving Intermediates of *Aspergillus nidulans* Isopenicillin N Synthase. *J. Am. Chem. Soc.* **2016**, *138*, 8862−8874.

(9) Fielding, A. J.; Lipscomb, J. D.; Que, L., Jr. Characterization of an O_2 Adduct of an Active Cobalt-Substituted Extradiol-Cleaving Catechol Dioxygenase. *J. Am. Chem. Soc.* **2012**, *134*, 796−799.

(10) Gunderson, W. A.; Zatsman, A. I.; Emerson, J. P.; Farquhar, E. R.; Que, L.; Lipscomb, J. D.; Hendrich, M. P. Electron Paramagnetic Resonance Detection of Intermediates in the Enzymatic Cycle of an Extradiol Dioxygenase. *J. Am. Chem. Soc.* **2008**, *130*, 14465−14467.

(11) Deville, C.; Padamati, S. K.; Sundberg, J.; McKee, V.; Browne, W. R.; McKenzie, C. J. O_2 Activation and Double C-H Oxidation by a Mononuclear Manganese(II) Complex. *Angew. Chem., Int. Ed.* **2016**, *55*, 545−549.

(12) Coggins, M. K.; Sun, X.; Kwak, Y.; Solomon, E. I.; Rybak-Akimova, E.; Kovacs, J. A. Characterization of Metastable Intermediates Formed in the Reaction between a Mn(II) Complex and Dioxygen, Including a Crystallographic Structure of a Binuclear Mn(III)−Peroxo Species. *J. Am. Chem. Soc.* **2013**, *135*, 5631−5640.

(13) (a) Shook, R. L.; Peterson, S. M.; Greaves, J.; Moore, C.; Rheingold, A. L.; Borovik, A. S. Catalytic Reduction of Dioxygen to Water with a Monomeric Manganese Complex at Room Temperature. *J. Am. Chem. Soc.* **2011**, *133*, 5810−5817. (b) Guo, M.; Lee, Y. M.; Gupta, R.; Seo, M. S.; Ohta, T.; Wang, H. H.; Liu, H. Y.; Dhuri, S. N.; Sarangi, R.; Fukuzumi, S.; Nam, W. Dioxygen Activation and O−O Bond Formation Reactions by Manganese Corroles. *J. Am. Chem. Soc.* **2017**, *139*, 15858−15867. (c) Sankaralingam, M.; Lee, Y. M.; Jeon, S. H.; Seo, M. S.; Cho, K. B.; Nam, W. A Mononuclear Manganese(III)−Hydroperoxo Complex: Synthesis by Activating Dioxygen and Reactivity in Electrophilc and Nucleophilic Reactions. *Chem. Commun.* **2018**, *54*, 1209−1212.

(14) Chiang, C. W.; Kleespies, S. T.; Stout, H. D.; Meier, K. K.; Li, P. Y.; Bominaar, E. L.; Que, L., Jr.; Münck, E.; Lee, W. Z. Characterization of a Paramagnetic Mononuclear Nonheme Iron-Superoxo Complex. *J. Am. Chem. Soc.* **2014**, *136*, 10846−10849.

(15) (a) Hong, S.; Sutherlin, K. D.; Park, J.; Kwon, E.; Siegler, M. A.; Solomon, E. I.; Nam, W. Crystallographic and Spectroscopic Characterization and Reactivities of a Mononuclear Non-Haem Iron(III)-Superoxo Complex. *Nat. Commun.* **2014**, *5*, 5440−5547. (b) Blakely, M. N.; Dedushko, M. A.; Yan Poon, P. C.; Villar-Acevedo, G.; Kovacs, J. A. Formation of a Reactive, Alkyl Thiolate-Ligated Fe^{III}-Superoxo Intermediate Derived from Dioxygen. *J. Am. Chem. Soc.* **2019**, *141*, 1867. (c) Noh, H.; Cho, J. Synthesis, Characterization and Reactivity of Non-Heme 1st Row Transition Metal-Superoxo Intermediates. *Coord. Chem. Rev.* **2019**, *382*, 126−144.

(16) Wang, C. C.; Chang, H. C.; Lai, Y. C.; Fang, H.; Li, C. C.; Hsu, H. K.; Li, Z. Y.; Lin, T. S.; Kuo, T. S.; Neese, F.; Ye, S.; Chiang, Y. W.; Tsai, M. L.; Liaw, W. F.; Lee, W. Z. Structurally Characterized Nonheme Cobalt−Hydroperoxo Complex Derived from Its Superoxo Intermediate via Hydrogen Atom Abstraction. *J. Am. Chem. Soc.* **2016**, *138*, 14186−14189.

(17) Oddon, F.; Chiba, Y.; Nakazawa, J.; Ohta, T.; Ogura, T.; Hikichi, S. Characterization of Mononuclear Non-heme Iron(III)-Superoxo Complex with a Five-Azole Ligand Set. *Angew. Chem., Int. Ed.* **2015**, *54*, 7336−7339.

(18) (a) Sacramento, J. J. D.; Goldberg, D. P. The hydrogen atom transfer reactivity of a porphyrinoid cobalt superoxide complex. *Chem. Commun.* **2019**, *55*, 913−916. (b) Bajdor, K.; Nakamoto, K.; Kanatomi, H.; Murase, I. Resonance Raman Spectra of Molecular Oxygen Adducts of Co(salen) and Its Derivatives in Solution. *Inorg. Chim. Acta* **1984**, *82*, 207−210.

(19) Liu, L. L.; Li, H. X.; Wan, L. M.; Ren, Z. G.; Wang, H. F.; Lang, J. P. Mn(III)−Superoxo Complex of a Zwitterionic Calix[4]arene with an Unprecedented Linear End-On Mn(III)−O_2 Arrangement and Good Catalytic Performance for Alkene Epoxidation. *Chem. Commun.* **2011**, *47*, 11146−11148.

(20) (a) Woertink, J. S.; Tian, L.; Maiti, D.; Lucas, H. R.; Himes, R. A.; Karlin, K. D.; Neese, F.; Würtele, C.; Holthausen, M. C.; Bill, E.; Sundermeyer, J.; Schindler, S.; Solomon, E. I. Spectroscopic and Computational Studies of an End-on Bound Superoxo-Cu(II) Complex: Geometric and Electronic Factors That Determine the Ground State. *Inorg. Chem.* **2010**, *49*, 9450−9459. (b) Zhang, X.; Furutachi, H.; Fujinami, S.; Nagatomo, S.; Maeda, Y.; Watanabe, Y.; Kitagawa, T.; Suzuki, M. Structural and Spectroscopic Characterization of (μ-Hydroxo or μ-Oxo)(μ-peroxo) diiron(III) Complexes: Models for Peroxo Intermediates of Non-Heme Diiron Proteins. *J. Am. Chem. Soc.* **2005**, *127*, 826−827.

(21) Schatz, M.; Raab, V.; Foxon, S. P.; Brehm, G.; Schneider, S.; Reiher, M.; Holthausen, M. C.; Sundermeyer, J.; Schindler, S. Combined Spectroscopic and Theoretical Evidence for a Persistent End-On Copper Superoxo Complex. *Angew. Chem., Int. Ed.* **2004**, *43*, 4360−4363.

(22) Peterson, R. L.; Himes, R. A.; Kotani, H.; Suenobu, T.; Tian, L.; Siegler, M. A.; Solomon, E. I.; Fukuzumi, S.; Karlin, K. D. Cupric Superoxo-Mediated Intermolecular C-H Activation Chemistry. *J. Am. Chem. Soc.* **2011**, *133*, 1702−1705.

(23) Cho, J.; Woo, J.; Nam, W. An "End-On" Chromium(III)-Superoxo Complex: Crystallographic and Spectroscopic Characterization and Reactivity in C-H Bond Activation of Hydrocarbons. *J. Am. Chem. Soc.* **2010**, *132*, 5958−5959.

(24) Bencini, A.; Gatteschi, D. *Electron Paramagnetic Resonance of Exchange Coupled Systems*; Sringer-Verlag: Berlin, 1990.

(25) (a) Krzystek, J.; Ozarowski, A.; Telser, J. Multi-Frequency, High-Field EPR as a Powerful Tool to Accurately Determine Zero-Field Splitting in High-Spin Transition Metal Coordination Complexes. *Coord. Chem. Rev.* **2006**, *250*, 2308−2324. (b) Orio, M.; Pantazis, D. A.; Petrenko, T.; Neese, F. Magnetic and

DOI: 10.1021/acs.inorgchem.9b00767
Inorg. Chem. 2019, 58, 9756−9765

Spectroscopic Properties of Mixed Valence Manganese(III,IV) Dimers: A Systematic Study Using Broken Symmetry Density Functional Theory. *Inorg. Chem.* **2009**, *48*, 7251.
(26) Duboc, C. Determination and Prediction of the Magnetic Anisotropy of Mn Ions. *Chem. Soc. Rev.* **2016**, *45*, 5834−5847.
(27) (a) Mair, R. D.; Graupner, A. J. Determination of Organic Peroxides by Iodine Liberation Procedures. *Anal. Chem.* **1964**, *36*, 194−201. (b) Das, D.; Lee, Y.-M.; Ohkubo, K.; Nam, W.; Karlin, K. D.; Fukuzumi, S. Acid-Induced Mechanism Change and Overpotential Decrease in Dioxygen Reduction Catalysis with a Dinuclear Copper Complex. *J. Am. Chem. Soc.* **2013**, *135*, 4018−4026.
(28) Gupta, R.; Taguchi, T.; Borovik, A. S.; Hendrich, M. P. Characterization of Monomeric $Mn^{II/III/IV}$−Hydroxo Complexes from X- and Q-Band Dual Mode Electron Paramagnetic Resonance (EPR) Spectroscopy. *Inorg. Chem.* **2013**, *52*, 12568−12575.
(29) Luo, Y.-R. *Handbook of Bond Dissociation Energies in Organic Compounds*; CRC Press: Boca Raton, FL, 2002.
(30) Tano, T.; Okubo, Y.; Kunishita, A.; Kubo, M.; Sugimoto, H.; Fujieda, N.; Ogura, T.; Itoh, S. Redox Properties of a Mononuclear Copper(II)-Superoxide Complex. *Inorg. Chem.* **2013**, *52*, 10431−10437.
(31) Kindermann, N.; Gunes, C. J.; Dechert, S.; Meyer, F. Hydrogen Atom Abstraction Thermodynamics of a μ-1,2-Superoxo Dicopper(II) Complex. *J. Am. Chem. Soc.* **2017**, *139*, 9831−9834.
(32) Bailey, W. D.; Dhar, D.; Cramblitt, A. C.; Tolman, W. B. Mechanistic Dichotomy in Proton-Coupled Electron-Transfer Reactions of Phenols with a Copper Superoxide Complex. *J. Am. Chem. Soc.* **2019**, *141*, 5470−5480.
(33) (a) Zhang, Y.-X.; Du, D.-M.; Chen, X.; Lü, S.-F.; Hua, W.-T. Enantiospecific Synthesis of Pyridinylmethyl Pyrrolidinemethanols and Catalytic Asymmetric Borane Reduction of Prochiral Ketones. *Tetrahedron: Asymmetry* **2004**, *15*, 177−182. (b) Mader, E. A.; Larsen, A. S.; Mayer, J. M. Hydrogen Atom Transfer from Iron(II)-Tris[2,2′-bi(tetrahydropyrimidine)] to TEMPO: A Negative Enthalpy of Activation Predicted by the Marcus Equation. *J. Am. Chem. Soc.* **2004**, *126*, 8066−8067. (c) Park, J. K.; Lee, H. G.; Bolm, C.; Kim, B. M. Asymmetric Diethyl- and Diphenylzinc Additions to Aldehydes by Using a Fluorine-Containing Chiral Amino Alcohol: A Striking Temperature Effect on the Enantioselectivity, a Minimal Amino Alcohol Loading, and an Efficient Recycling of the Amino. *Chem. - Eur. J.* **2005**, *11*, 945−950.
(34) Stoll, S.; Schweiger, A. EasySpin, a Comprehensive Software Package for Spectral Simulation and Analysis in EPR. *J. Magn. Reson.* **2006**, *178*, 42−55.
(35) (a) Becke, A. D. Density-Fnnctional Exchange-Energy Approximation with Correct Asymptotic Behavior. *Phys. Rev. A: At., Mol., Opt. Phys.* **1988**, *38*, 3098−3100. (b) Lee, C.; Yang, W.; Parr, R. G. Development of the Colic-Salvetti Correlation-Energy Formula into a Functional of the Electron Density. *Phys. Rev. B: Condens. Matter Mater. Phys.* **1988**, *37*, 785−789.
(36) Schäfer, A.; Huber, C.; Ahlrichs, R. Fully Optimized Contracted Gaussian Basis Sets of Triple Zeta Valence Quality for Atoms Li to Kr. *J. Chem. Phys.* **1994**, *100*, 5829−5835.
(37) Schäfer, A.; Horn, H.; Ahlrichs, R. Fully Optimized Contracted Gaussian Basis Sets for Atoms Li to Kr. *J. Chem. Phys.* **1992**, *97*, 2571−2577.
(38) Eichkorn, K.; Weigend, F.; Treutler, O.; Ahlrichs, R. Auxiliary Basis Sets for Main Row Atoms and Transition Metals and Their Use to Approximate Coulomb Potentials. *Theor. Chem. Acc.* **1997**, *97*, 119−124.
(39) Eichkorn, K.; Treutler, O.; Öhm, H.; Häser, M.; Ahlrichs, R. Auxiliary Basis Sets to Approximate Coulomb Potentials. *Chem. Phys. Lett.* **1995**, *240*, 283−290.
(40) Tomasi, J.; Mennucci, B.; Cammi, R. Quantum Mechanical Continuum Solvation Models. *Chem. Rev.* **2005**, *105*, 2999−3093.
(41) Grimme, S.; Ehrlich, S.; Goerigk, L. Effect of the Damping Function in Dispersion Corrected Density Functional Theory. *J. Comput. Chem.* **2011**, *32*, 1456−1465.
(42) Staroverov, V. N.; Scuseria, G. E.; Tao, J.; Perdew, J. P. Comparative Assessment of a New Nonempirical Density Functional: Molecules and Hydrogen-Bonded Complexes. *J. Chem. Phys.* **2003**, *119*, 12129−12137.
(43) Neese, F. Prediction and Interpretation of the ^{57}Fe Isomer Shift in Mössbauer Spectra by Density Functional Theory. *Inorg. Chim. Acta* **2002**, *337*, 181−192.
(44) Orio, M.; Pantazis, D. A.; Petrenko, T.; Neese, F. Magnetic and Spectroscopic Properties of Mixed Valence Manganese(III,IV) Dimers: A Systematic Study Using Broken Symmetry Density Functional Theory. *Inorg. Chem.* **2009**, *48*, 7251−7260.
(45) Neese, F.; Solomon, E. I. Calculation of zero-field splittings, g-values, and the relativistic nephelauxetic effect in transition metal complexes. Application to high-spin ferric complexes. *Inorg. Chem.* **1998**, *37*, 6568−6582.
(46) Sinnecker, S.; Neese, F.; Noodleman, L.; Lubitz, W. Calculating the Electron Paramagnetic Resonance Parameters of Exchange Coupled Transition Metal Complexes Using Broken Symmetry Density Functional Theory: Application to a Mn^{III}/Mn^{IV} Model Compound. *J. Am. Chem. Soc.* **2004**, *126*, 2613−2622.
(47) Neese, F. Calculation of the Zero-Field Splitting Tensor on the Basis of Hybrid Density Functional and Hartree-Fock Theory. *J. Chem. Phys.* **2007**, *127*, 164112.
(48) Mcweeny, R.; Mizuno, Y. The Density Matrix in Many-Electron Quantum Mechanics. II. Separation of Space and Spin Variables; Spin Coupling Problems. *Proc. R. Soc. London A* **1961**, *259*, 554−577.
(49) Sinnecker, S.; Neese, F. Spin-Spin Contributions to the Zero-Field Splitting Tensor in Organic Triplets, Carbenes and Biradical-A Density Functional and Ab Initio Study. *J. Phys. Chem. A* **2006**, *110*, 12267−12275.
(50) (a) Neese, F. The ORCA program system. *WIREs Comput. Mol. Sci.* **2012**, *2*, 73−78. (b) Neese, F. Software update: the ORCA program system, version 4.0. *WIREs Comput. Mol. Sci.* **2018**, *8*, e1327.

DOI: 10.1021/acs.inorgchem.9b00767
Inorg. Chem. 2019, 58, 9756−9765